RESEARCH ARTICLE





Toward a new conceptual model for groundwater flow in merokarst systems: Insights from multiple geophysical approaches

Pamela L. Sullivan¹ | Chi Zhang² | Michael Behm³ | Fan Zhang² | G. L. Macpherson²

Correspondence

Pamela L. Sullivan, College of Earth, Ocean, and Atmospherics Science, Oregon State University, Corvallis OR 97331. Email: pamela.sullivan@oregonstate.edu

Funding information

Konza Prairie Long Term Ecological Research (LTER) grant, Grant/Award Number: NSF 1440484

Abstract

Merokarst aquifers - relatively thin (<1-2 m) karstified carbonate units interbedded between mudstone, shale, or sandstone - constitute a significant proportion of carbonate terrain and underlie a large portion of the west- and south-central USA, yet few advances have been made in our understanding of porosity development and flow-path generation in these complex systems in decades. Toward this end, we used a multi-geophysical approach at the well-studied Konza Prairie Biological Station (KPBS), a part of the larger Flint Hills (25,734 km²), underlain by thin limestone units (1-2 m thick) interbedded with mudstone/shale units (2-4 m thick), to elucidate hydrologic connectivity and potential controls on known groundwater flow directions. We combined electrical resistivity tomography (ERT), surface and borehole nuclear magnetic resonance (NMR), and ground penetrating radar (GPR) measurements across a low order catchment where over 25 boreholes and groundwater wells sampling perched aquifers could be used to constrain interpretation of lithology, potential flow paths, and permeability. Data revealed that groundwater export may be an unappreciated component of lateral-flow-dominated models used to represent merokarst in that: (a) potentiometric surfaces from two limestone units showed groundwater flows toward a hydrologic depression, opposite the direction of stream flow, in the upstream portion of the catchment, (b) long term measures of groundwater levels revealed a greater variance and overall water storage in this same upstream area compared to wells near the outlet, and (c) ERT and NMR results indicate pronounced lateral heterogeneity within a given unit, suggestive of a greater degree of vertical hydrological connectivity than usually considered for horizontally-layered merokarst. Our data suggest vertical connectivity can shunt water to depth in these "sandwiched" merokarst aquifers, yielding atypical groundwater flow directions and unrealized deep export of weathering solutes and carbon.

critical zone, electrical resistivity, hydrogeophysics, merokarst, surface/borehole nuclear magnetic resonance

¹College of Earth, Ocean, and Atmospherics Science, Oregon State University, Corvallis, Oregon

²Department of Geology, University of Kansas, Lawrence, Kansas

³School of Geosciences, Oklahoma University, Norman Oklahoma

1 | INTRODUCTION

Understanding the mechanisms that drive the heterogeneous porosity development and the resultant high hydraulic conductivity of carbonate terrains is imperative for developing process-based representations of vadose zone-groundwater interaction and groundwater flow (e.g., Hartmann, Goldscheider, Wagener, Lange, & Weiler, 2014; Malagò et al., 2016; Phillips, 2018) that can be used to elucidate the impacts of future climatic and land use/cover change on water resources in carbonate systems (Martin & White, 2008; Sullivan, Macpherson, Martin, & Price, 2019). To date numerous efforts have been made to advance our understanding of karst systems (e.g., Ford & Williams, 2013; White, 1969), with much of the energy focused on conceptualizing porosity generation and flow paths in massive units. Here dissolution processes govern the generation of vertical conduits down toward the location of the water table or perched water table where larger, horizontal conduits and caves develop. As climate and uplift alter the position of the water table over time, other large horizontal conduits/ caves initiate (Dreybrodt, 2012; Plan, Filipponi, Behm, Seebacher, & Jeutter, 2009). Given this conceptual model, many statistical and numerical models have been derived to predict hydrologic response of karst environments (e.g., Hartmann, Lange, Weiler, Arbel, & Greenbaum, 2012; Malagò et al., 2016).

"Sandwich" carbonate aguifers or merokarst — thin impure carbonate units that contain karst features interbedded between mudstones. shales, or sandstones (Dreybrodt, 2012; White, 1969) - remain a fairly understudied carbonate terrain, with little advance in the development of conceptual models of porosity distribution and flow paths since White (1969). However, they constitute a significant proportion of carbonate terrains and underlie a large portion of the west- and south- central USA (e.g., Weary & Doctor, 2014). White suggested that karst features in these systems lie mainly in the horizontal plane of the carbonate beds, similar to a road network, and that this generation of secondary porosity is mainly driven by horizontal infiltration of unequilibrated stream water into and out of the unit, with little vertical connection or flow between these interbedded limestone units. As base level changes, the connection of the stream to the unit changes as well and karst development slows as the units become disconnected from the stream. Given the natural development of karst features and their ability to develop collapse features and sink holes, this idea of predominantly horizontal flow should be considered the initial and simplest merokarst geometry, with more complicated three-dimensional flow paths developing as the system weathers. For example, emerging data from the Flint Hills merokarst region of the USA (25,734 km², eastern Kansas and northern Oklahoma), shows groundwater levels that indicate opposing groundwater flow directions in layered limestone units (characteristic of merokarst) (Macpherson, 1996), which may develop as a result of vertical connectivity in these nearly flat-lying limestone units. These data suggest the conceptual model of porosity development and flow paths in merokarst may need more scrutiny, especially in the context of landscape development.

Geophysical techniques can be used to infer spatial and temporal variations in subsurface properties. Collecting multiple types of

near-surface geophysical measurements (Holbrook et al., 2014; Parsekian, Singha, Minsley, Holbrook, & Slater, 2015; Robinson et al., 2008) have helped address questions on how subsurface structure governs water availability as well as water and chemical fluxes through the critical zone (Grant & Dietrich, 2017). These advancing geophysical data processing and interpretation capabilities are leading to the emergence of new conceptual and numerical critical zone models (e.g., Fan, 2015; Fan et al., 2019). Given that electrical resistivity tomography (ERT) and GPR have been used in massive limestone units (holokarst) to locate karst conduits, sinkholes and fractures (Carrière, Chalikakis, Sénéchal, Danquigny, & Emblanch, 2013; Leucci, Margiotta, & Negri, 2004), it is likely that such geophysical tools may also help reveal hydrologic connectivity and variability of hydrological properties related to water storage and transmission in merokarst. This is especially true if a site's geologic structure (e.g., lithology, mineralogy, dip) can be constrained with additional data such as borehole logs, knowledge of groundwater table dynamics, or soil pit data.

Our goal here is to update the conceptual model of secondary porosity distribution and flow in merokarst using multi-geophysical tools. We link together ERT, surface and borehole nuclear magnetic resonance (sNMR and bNMR), and ground penetrating radar (GPR) in the same location where data can be validated with borehole logs, groundwater pumping/slug tests, known water levels, and water table responses. We rely on ERT to provide lateral and vertical variation of specific electrical resistivity with high resolution to identify potential vertical hydrologic connections. We validate these findings at point locations using NMR, which constrains water content and its degree of mobility (e.g., Coates, Xiao, & Prammer, 1999). GPR, in conjunction with ERT, characterizes lateral variations in the shallow subsurface (e.g., Al-fares, Bakalowicz, Guérin, & Dukhan, 2002). We specifically focus on the KPBS, a well-studied merokarst area in the larger Flint Hill region, where more than 25 boreholes and 29 years of hydrologic monitoring can be used to constrain and calibrate near-surface geophysical measurements. The story that emerges from these data is that vertical connectivity between limestone units is greater than currently recognized; supporting a deep, unaccounted for, groundwater export component in merokarst conceptual models.

2 | STUDY AREA

The 35 km² Konza Prairie Biological Station (KPBS) is located in the Flint Hills Physiographic Province (25,734 km²), northeastern Kansas (Figure 1), and is underlain by widespread Permian-aged units of the central US. The Permian rocks comprise limestone (1–2 m thick) interbedded with mudstone/shale (2–4 m thick), rendering it merokarst. Hydrogeochemical evidence of flashy hydrographs (Costigan, Daniels, & Dodds, 2015), quick groundwater table response times to precipitation events (Brookfield, Macpherson, & Covington, 2017), and distinct groundwater chemistry and hydraulic heads in each of the layered limestone units supports its characterization as merokarst with perched aquifers (Macpherson, 1996). The stratigraphy is nearly flat-lying (dip 0.1–0.2°NW; Smith, 1991) and the field

FIGURE 1 Groundwater monitoring wells (blue dots) located in the NO4d watershed Konza Prairie Biological Station and Long-Term Ecological Research (LTER) site (Kansas, USA). Stream in right panel is designated by light blue

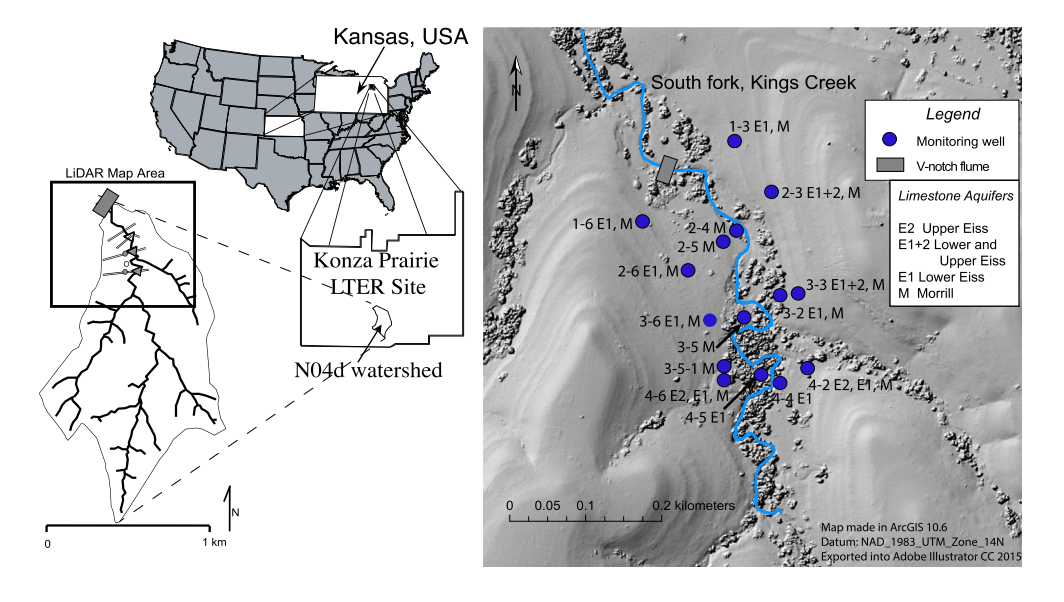
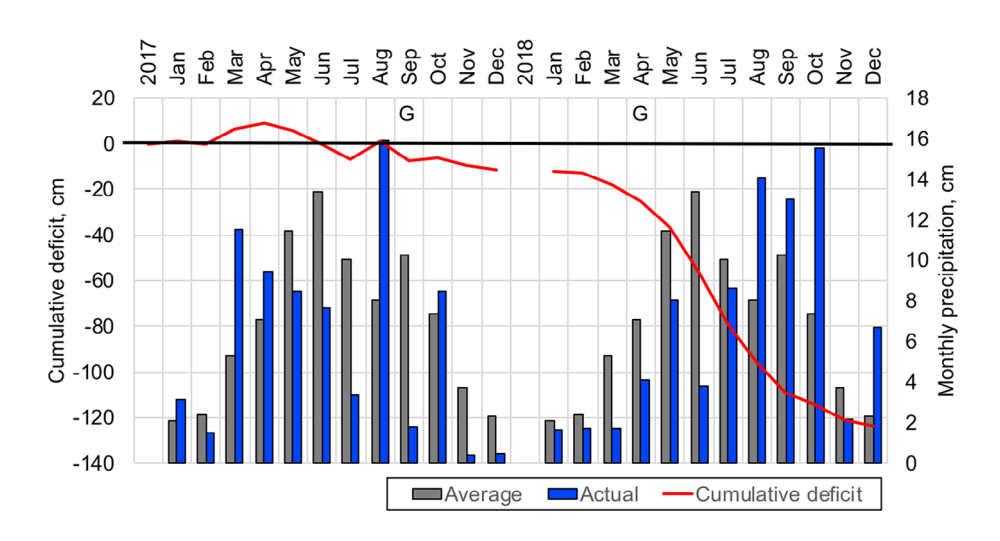


FIGURE 2 Monthly average precipitation (1983–2017) at Konza Biological Station (grey bars; headquarters weather station) compare to the actual monthly precipitation (blue) in 2017–2018. Red line demonstrates the cumulative deficit in precipitation over this two-year period. "G" indicates the months when the two geophysical surveys were completed. Both surveys were completed during dry periods. (Climate and Hydrology Database Projects, https://climhy.lternet.edu/)



site, the lower fourth of the 1.2 km² N04d watershed, like the rest of the Flint Hills, has deeply dissected hills (60 m of relief, slope gradients up to 25%) with bench and slope topography enforced by more resistant limestones (benches) and weathered shales (slopes). Lower Permian-aged Florence Limestone Member of the Barnestone Limestone caps the stratigraphic units at the ridgetops and is followed in sequence six mudstone units and six limestone units, with the Cottonwood Limestone Member (Cottonwood) of the Beattie Limestone cropping out below the triangle-fluted flume of the N04d watershed (Figure 1). Limestone units are mainly calcite with traces of dolomite (Macpherson et al., 2008), while the mudstones are dominated by illite, chlorite, and mixed-layer clays of chlorite-illite and chloritevermiculite (see Macpherson & Sullivan, 2018 for details). Soils at Konza that mantle the bedrock are predominantly silty-clay loams (Ransom, Rice, Todd, & Wehmueller, 1998) and are thin on the ridgetops (<20-50 cm) and thicken (~2 m) downslope.

The climate at Konza is classified as mesic with average annual precipitation and air temperature of \sim 835 mm and 13°C, respectively (Hayden, 1998; Nippert & Knapp, 2007). When the geophysical

surveys were conducted (September 2017 and April 2018), precipitation was below average with 721 mm observed in 2017 (86% of the annual average) and 51% of average for January through March of 2018, with only 2.9 mm observed prior to the April 2018 survey (see blue bars in Figure 2). Together this resulted in a cumulative deficit (since January 2017) of \sim 7 cm in September 2017 and \sim 18 cm in April 2018 (see red line Figure 2).

3 | HYDROGEOLOGICAL SETTING AND PRELIMINARY CONCEPTUAL MODEL

Where the geophysical surveys were run, outcropping geologic units range from the Threemile Limestone Member (Wreford Limestone) near the hilltops to the Cottonwood cropping out below the triangle-fluted flume. Our focus is the land surface to the Morrill Limestone Member of the Beattie Limestone (Morrill or M; average thickness and top elevation of 1.1 m and 365.6 m, respectively) as well as the underlying Cottonwood (average thickness and top elevation of

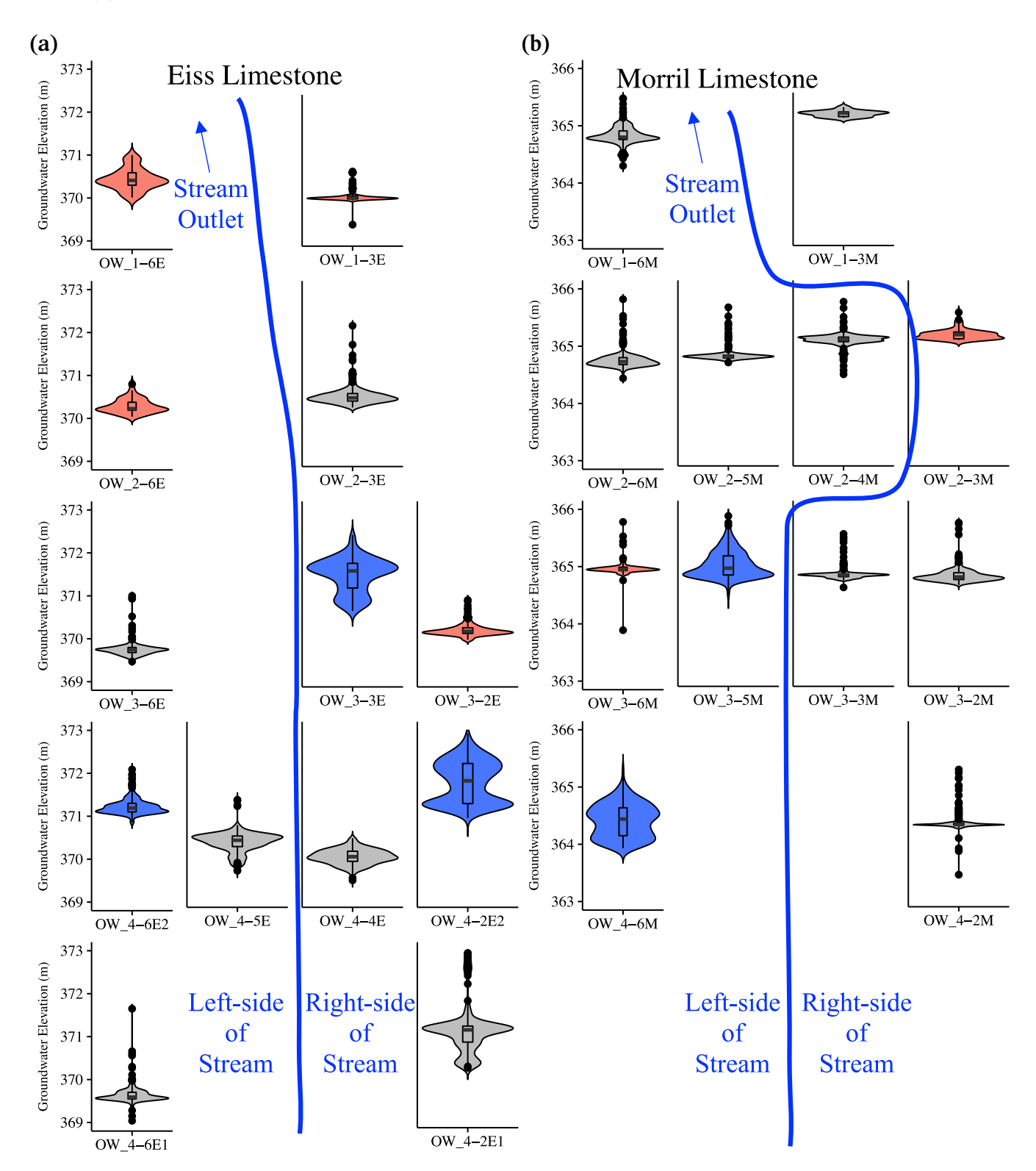


FIGURE 3 Violin plots of the distribution of the groundwater elevation in the Eiss (a) and Morrill (b) limestone units at Konza. Observation wells (OW) are aligned in accordance to their position in the transects and relative location to the stream (blue line)—not the actual stream position—: transect 1 (top row) is closest to the outlet of the catchment. Nested within each violin plot is a box plot representing the mean (black) and one standard deviation from the mean (whiskers), with black dots representing the outliers (>1 standard deviation from the mean). Wells that went dry for >30% of the observations are indicated in light red, while wells with a known high hydraulic conductivity (>10⁻⁵ m s⁻¹) are indicated in blue

1.75 m and 361.8 m, respectively). Monitoring wells are completed in three units. Along the geophysical transects, monitoring wells in the stratigraphically oldest unit are completed in the Morrill. Wells that sample the stratigraphically youngest unit are completed in the upper part of the Eiss Limestone Member of the Bader Limestone (Upper Eiss or E2), lower part of the Eiss Limestone Member (Lower Eiss or E1), or in the undifferentiated Eiss Limestone (Eiss). The saturated hydraulic conductivity (K_{h-sat} ; Table S1) of the Morrill and Eiss limestones are consistent with karstified, thick limestones ($10^{-6}-10^{-2}$ m/s) and of limestone and dolomite ($10^{-11}-10^{-5}$ m/s; Lewis et al., 2006): where the highest K_{h-sat} occurs in the Morrill near the upstream portion of the well field (e.g., 3-5M, 4-6M; $10^{-3}-10^{-5}$ m/s; blue fill Figure 3), while the Upper Eiss wells also have consistently higher K_{h-sat} ($10^{-3}-10^{-5}$ m/s) compared to the Lower Eiss wells ($10^{-7}-10^{-8}$; e.g., 4-6E1 and 4-2E1; blue fill panel a Figure 3).

Monthly groundwater level measurements (1990-2019) from 25 of the 35 wells in the NO4d catchment at Konza reveal an interesting pattern in the groundwater elevation distribution (Violin plots; Figure 3) with the water table elevation \sim 4 m higher in the Eiss than the Morrill. Three patterns were observed: (a) narrow distributionlittle variability in groundwater elevation-(45% of wells; e.g., 1-3E and 1-3M in top right Figure 3), (b) medium distribution-slightly larger variability in groundwater table-(28% of wells; e.g., 1-6E and 1-6M top left Figure 3), and (c) wide distributions—greatest variability in groundwater elevation-(27% of wells, 3-3E and 3-5M). Pairing these data with frequency of "dry well" observations (light red fill if >30%, Figure 3) and measures of hydraulic conductivity, spatial patterns emerge: (a) limestones dry more frequently, especially the Eiss limestone, are closer to the outlet, (b) greater variability in water table elevation and higher hydraulic conductivities occur upstream. (c) hydraulic gradients close to the outlet are generally much lower than in upstream sections, and (d) flow lines inferred from potentiometric surfaces (see Figure S1) of the Eiss limestone are parallel to topographic gradients—flow is toward the stream—close to the outlet, but upstream, groundwater flows toward a hydraulic depression, while in Morrill limestone groundwater everywhere appears to flow toward the same upstream hydraulic depression (i.e., reverse to the stream flow). This hydraulic depression, which was recently confirmed using dye tracing (Barry, 2018), may be a collapse feature in the south-central part of the study area. The dye trace also revealed a strong vertical connection, exact location unknown, that allows downward movement of groundwater at least to the next lower limestone below the observation wells, the Cottonwood.

4 | GEOPHYSICAL METHODS, DATA ACQUISITION, DATA PROCESSING

To examine hydrologic connectivity of merokarst at Konza we used three geophysical tools (ERT, NMR, and GPR; fundamental aspects outlined in Appendix S1). When possible, measurements were collected at the identical locations (Figure 4) where borehole and well data could be used to constrain the geophysical results. Specifically,

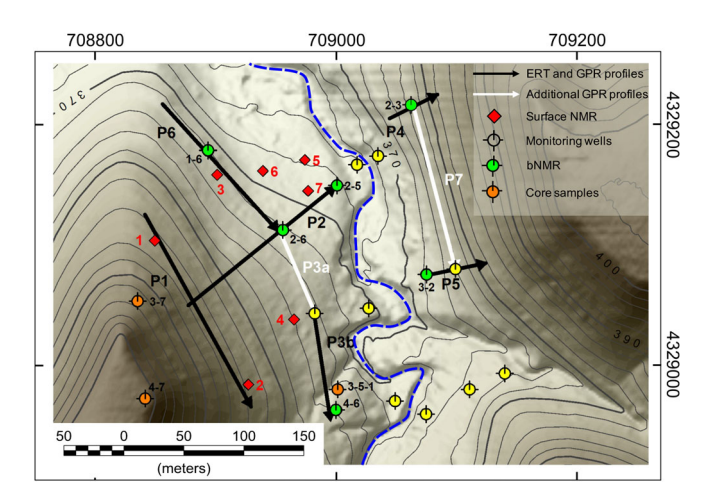


FIGURE 4 Locations of groundwater wells (circles with cross hairs) and geophysical measurements conducted in the merokarst of Konza in the NO4d catchment superimposed on a digital terrain model (elevation in metres ASL). Black soild lines represent the six profiles where ERT and GPR surveys were both conducted. Two additional GPR surveys were conducted and represented by the white lines (P3a and P7). Red diamonds labelled 1–7 mark the locations where sNMR measurements were conducted. Wells coloured green (i.e., 1–6, 2–6, 2–3, 2–5, 3–2, and 4–6) indicate where bNMR were collected. Wells coloured orange indicate where detailed core information was available for constraining geophysical interpretations, while yellow coloured wells only had driller information on cuttings. Blue dashed line marks the location of the intermittent stream

the well data allow us to interpolate elevation surfaces of the formations (see Figure S2) based on the knowledge of lithology from cores/cutting and the small stratigraphic dips of the well-established layer-cake stratigraphy. Line surveys (ERT and GPR) were conducted to cross boreholes in two orientations: perpendicular to the stream (e.g., P2, P4, and P5; Figure 4), and parallel to the stream (e.g., P1, P3b, and P6; Figure 4). Perpendicular transects crossed multiple limestone layers, while stream-parallel transects permit us to explore variability within given units of this layer-cake lithology. The ERT, sNMR, and GPR data were collected in September 2017, while the bNMR data were collected in April 2018. In both instances, Konza was experiencing a cumulative deficit in precipitation, though this deficit was much greater in April (Figure 2). When interpreting data from these two time periods we expect the bNMR data will reflect a drier hydrologic state.

4.1 | ERT profiles

A total of six ERT profiles were conducted at Konza (lower part of N04d) with lengths of ~ 50 to 175 m (Figure 4; Table S2). Four of the six surveys were located on the west side of the catchment (P1, 2, 3, and 6) and two were on the east side (P4 and 5). ERT data were acquired using the GF Instruments ARES-II system with stainless steel electrodes at a 1-m spacing. All profiles presented were measured using Wenner electrode configuration, which maximizes vertical

resolution in case of thin and flat layers, as expected in the Flint Hills. Two profiles were additionally measured using the dipole–dipole configuration (P4 and 5), which is more sensitive to lateral resistivity variations (Everett, 2013).

The ERT data were processed and inverted using AGI EarthImager™ 2D resistivity inversion and modelling software using the damped least square inversion method. The choice of the initial model and of the damping factor usually have the major effects on the inversion (Loke, Chambers, Rucker, Kuras, & Wilkinson, 2013). The damping factor controls the ratio of the data fit (i.e., RMS error) and the degree of detail obtained in the 2D model. We chose the apparent resistivity distributions (pseudo-sections) as the initial models and selected the same damping factor for all profiles. Overall a relatively low data misfit (<5%) is achieved after only a small number of iterations indicative of high-quality data (Table S2).

4.2 | sNMR surveys

Seven sNMR surveys were conducted (soundings 1-7, red diamonds in Figure 4) using a multichannel sNMR instrument VistaClara GMR system. A vertical distribution of volumetric water content and apparent relaxation time (T_2^*) were retrieved from the measurements. The T_2^* contains the information about mean pore size (Grunewald & Knight, 2011). It is worth noting that the T_2^* differs from true transverse relaxation time T_2 measured from borehole NMR by taking into account the inhomogeneity of local magnetic fields. It is safe to use T_2^* to represent true T_2 since Konza prairie has low magnetic susceptibility. To overcome the background EM noise, we used a figureeight-shaped noise reference loop (35 or 36 m) for digital noise cancellation. The long axis of the measurement and cancellation noise loops were in northwest-southeast direction, which was parallel to the direction of strongest EM noise source in the region (power lines). We used 10-16 stacks of recordings and 28 pulse moments ranging from 0.1 to 10 A second (A.s). After noise cancellation and staking, data sets were imported and processed within an open-source sNMR processing package MRSmatlab (Müller-Petke, Dlugosch, Lehmann-Horn, & Ronczka, 2015) using QT inversion scheme. The QT inversion is an iterative process that simultaneously fits all pulse moments, signal amplitudes, and relaxation time until the best pair of water content distribution and the relaxation time profile can be determined. An earth resistivity model was implemented and served as the initial model. When adjacent ERT measurements were available, they replaced the earth resistivity model, providing better constraint on the inversion. The approximate depth of investigation is estimated at where the diagonal values of the sensitivity matrix dropped to 0.5 (Mazzilli et al., 2016).

4.3 | bNMR logging

In April, 2018, a total of six bNMR logging measurements were completed in two hillslope positions on the west side of the stream

(from upstream to outlet: wells 4-6, 2-6, and 1-6), on the east side of the stream (from upstream to outlet: wells 3-2 and 2-3), as well as in the valley (well 2-5, west side of stream) (Figure 4). A DART (VistaCara) system was used with a data-collection interval of 0.25 or 0.5 m. The DART has a well-defined cylindrical NMR-sensitive zone that is a maximum of 15 cm from the tool surface. The DART is used to take measurements at two frequencies for each depth interval. Each frequency was collected using two recovery times (T_r) in order to optimize the signal quality for short relaxation ($T_r = 100$ ms), and to capture long relaxation ($T_r = 1,000 \text{ ms}$). The averaged stack numbers for $T_r = 100 \text{ ms}$ is 500-1,000, while for $T_r = 1,000 \text{ ms}$ is 30-50. The relaxation time series from two frequencies were then combined and filtered by applying the moving-average to increase the signalto-noise ratio (SNR) at the cost of reduced vertical resolution. Borehole NMR inversion was performed using GMR processing software (Walsh, 2008). The NMR relaxation time (T_2) is fit with a multiexponential function to produce a T_2 distribution. The water content, or porosity when saturated, is calculated as the initial amplitude of the exponential relaxation function.

4.4 | GPR surveys

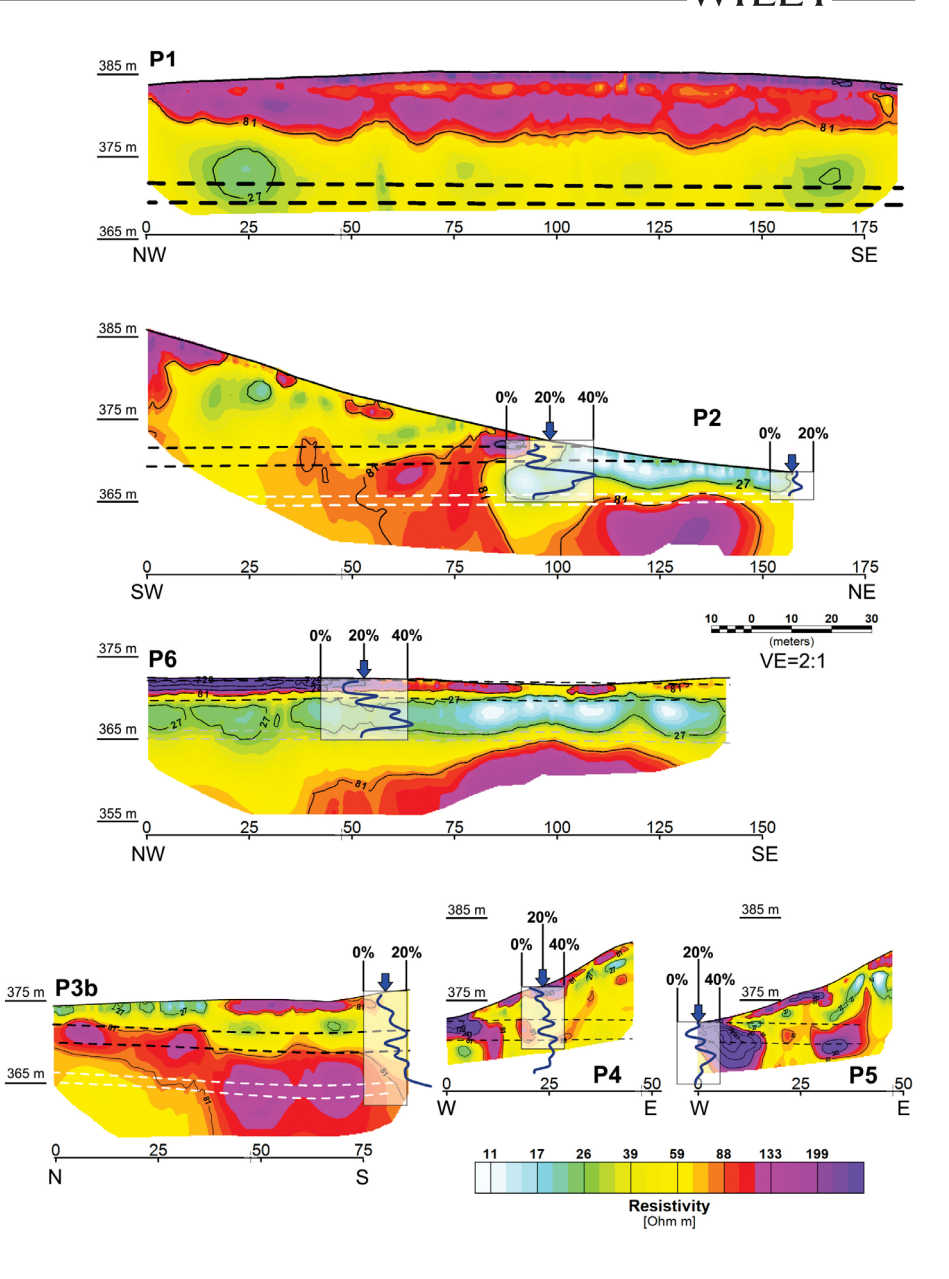
A total of seven zero-offset GPR surveys were conducted at Konza in September, 2017 (black and white lines, P1-7; Figure 4) using a Sensors & Software pulseEKKO Pro GPR with unshielded antennae (50, 100, 200 MHz). Lack of surface objects (e.g., trees, cars) minimized the potential negative impact of air wave reflections. The surveys revealed that the 200 MHz antenna with a spacing of 20 cm provides the most continuous image of reflectivity, therefore those data will be the focus of the results presented below. Data processing included dewow and frequency filtering (trapezoid bandpass filter 10–30–280–330 MHz), background removal, lateral smoothing, automatic gain control, and time-to-depth conversion with an assumed velocity of 0.1 m/ns. This standard velocity was chosen due to the absence of velocity information (e.g., diffractions) in the data. Migration is not effective due to the small dip angles (5–15°), coarse spatial sampling, low SNR, and the lack of velocity control.

5 | RESULTS AND DISCUSSION

5.1 | Electrical resistivity tomography (ERT)

We obtained resistivities that ranged between 10 Ω -m and 300 Ω -m for most locations, except for eastern transects P4 and P5 where significantly higher resistivities up to 5,000 Ω -m occur near the stream (Figure 5). In limestone, resistivity is largely governed by porosity and the fluid content occupying the voids: dry limestone can have resistivities from 1,000 to 10,000 Ω -m (Carrière et al., 2013; McCormack et al., 2017; Zhu, Currens, & Dinger, 2011) and fractured and/or saturated limestone can have resistivities from 20 to 500 Ω -m (Ammar & Kamal, 2018; Redhaounia, Ilondo, Gabtni, Sami, & Bédir, 2016;

FIGURE 5 The electrical resistivity distribution along the transects P1–P5 (see map in Figure 4 for locations). The water content determined from six bNMR measurements is plotted on ERT profiles. Note the logarithmic colour scale for resistivity values. Dashed black lines: tops and bottom of the Eiss Limestone. Dashed white lines: tops and bottom of the Morrill Limestone based on interpolation of well log data



Robert et al., 2011; Srinivasa Gowd, 2003). At the study site, ERT results superposed on the interpolated formation elevation maps (see Figure S2) show that the shale layers had low resistivities (10 Ω -m to 50 Ω -m) while the limestones had a wide range in resistivities (50 Ω -m to 5,000 Ω -m). Intriguingly, we also observed large ranges of resistivity within a given rock type (limestone or shale) and attribute these spatial resistivity variations to differences in the degree of water saturation, where high resistivity is associated with low saturation and vice versa (e.g., Figure 5 surveys P2 and P3b). Due to the intrinsic limited resolution of the method, the images of the resistivity distribution represent averages over wider areas and tend to be smeared, for example, high-resistivity zones of small extent will show up as larger blobs with intermediate resistivities. Further, sensitivity of inversion decreases with depth, and so deep, high-resistivity zones are likely to be underestimated in value (see Appendix S1: synthetic modelling).

To better understand the degree of vertical and lateral hydrologic connectivity we focus on two orientations of resistivity profiles at

Konza, those perpendicular to the stream (P2, P4, and P5; Figure 5) and those parallel to the stream (P1, P3b, and P6; Figure 5). Perpendicular transects crossed multiple limestone benches and exhibit complex patterns, illustrating both strong lateral and vertical variability, while stream-parallel profiles exhibited a more lateral homogeneity, mirroring the layer-cake lithology (P1 and P6; Figure 5). The only exception where strong vertical and lateral heterogeneity in resistivity was observed on a stream-parallel line was P3b. For streamperpendicular profiles and P3b, the significant degree of lateral heterogeneity within each unit is likely driven by differences in water content given similar lithology, and may be indicative of vertical hydrologic connectivity that can drain water from one lithologic unit to one below it. One interesting feature evident from the ERT profiles is the vertically flipped resistivity distribution in P2, P3b, P4, and P5. Where high resistivity units appeared on the surface, we observed areas of reduced resistivity that vertically cross both limestone and shale units. Such features present at distances of $\sim\!\!60$ and 125 m along P2, \sim 35 m along P3b, and at \sim 20 and 40 m along P4 and P5 (Figure 5). In contrast, stream-parallel profiles (P1and P6) exhibited little to no vertically flipped resistivity features—only slightly decreased resistivity region at \sim 55 and \sim 160 m in P1 and at \sim 90 and \sim 120 m in P6 (Figure 5). The vertical flipped features are an indication that water can be transmitted to depth, crossing both limestone and shale units in these areas. Surprisingly this suggests that shale units are likely helping to transmit water between limestone units, and it demonstrates the shale units have local enhanced permeability zones. Synthetic tests along profile P3b show that the flipped resistivity distribution is a robust feature and not an inversion artefact related to the lateral variation of surface resistivity (Appendix S1: synthetic modelling).

For transects P4 and P5 which are on the same hillslope separated by ~140 m, near-surface high resistivity (dry) zones mark the limestone outcrops of the Eiss limestone on the western edge of the stream. The upstream trend of more efficient groundwater transport in the limestones, evidenced by higher upstream hydraulic conductivity and more variable water-level elevations (Figure 3), may explain the higher resistivity observed in the more upstream P5 transect than the P4 transect, reflecting more complete water drainage during the dry study period. The overall patterns for these two stream-parallel profiles are fairly similar, for example lower resistivity in the Eiss limestone is observed with increased distance from the stream and from the outcrop on the hillside (eastward in both cases). This decrease in resistivity is also seen in limestone benches further upslope, and supports the hypothesis that the hydrogeologic regime is one of perched aguifers as interpreted from the consistently non-overlapping water table elevations in the limestones. The resistivity changes potentially identify where more moisture is retained (does not drain easily) because permeability is less developed and may indicate areas where limestone is less fractured/karstified. We note observations of split cores from wells at the site show more secondary porosity near the stream (3-5-1) than farther from the stream (e.g., visible voids decrease in order of 3-5-1 > 3-7 > 4-7; Figure S3), and again emphasize the higher range in water table elevation, fewer dry well episodes, and higher hydraulic conductivity determined by pumping/slug tests upstream than downstream (Section 3).

The heterogenous resistivity patterns in stream-parallel line P3b are intriguing and co-occur with the water table depression interpreted from hydraulic head in this area (information from well 3-6 and 4-6 helps to constrain interpolations; Figure S1). The northern part of transect P3b is overlain by colluvial clay deposits and also has low resistivity (potentially indicating more moisture), while the Eiss limestone directly below has high resistivity values followed by lower resistivity values in the even deeper Morrill limestone. The opposite holds true for observed resistivity in the southern portion of the transect, where the lower resistivities of the Eiss can be attributed to higher water content, which is confirmed by detectable groundwater levels in well 4-6 and bNMR measurement in the same well at the southern end (Figure 5). Well test data from this area (3-5-1 and 4-6) also reveal that Eiss and Morrill limestone are more hydrologically conductive in this area.

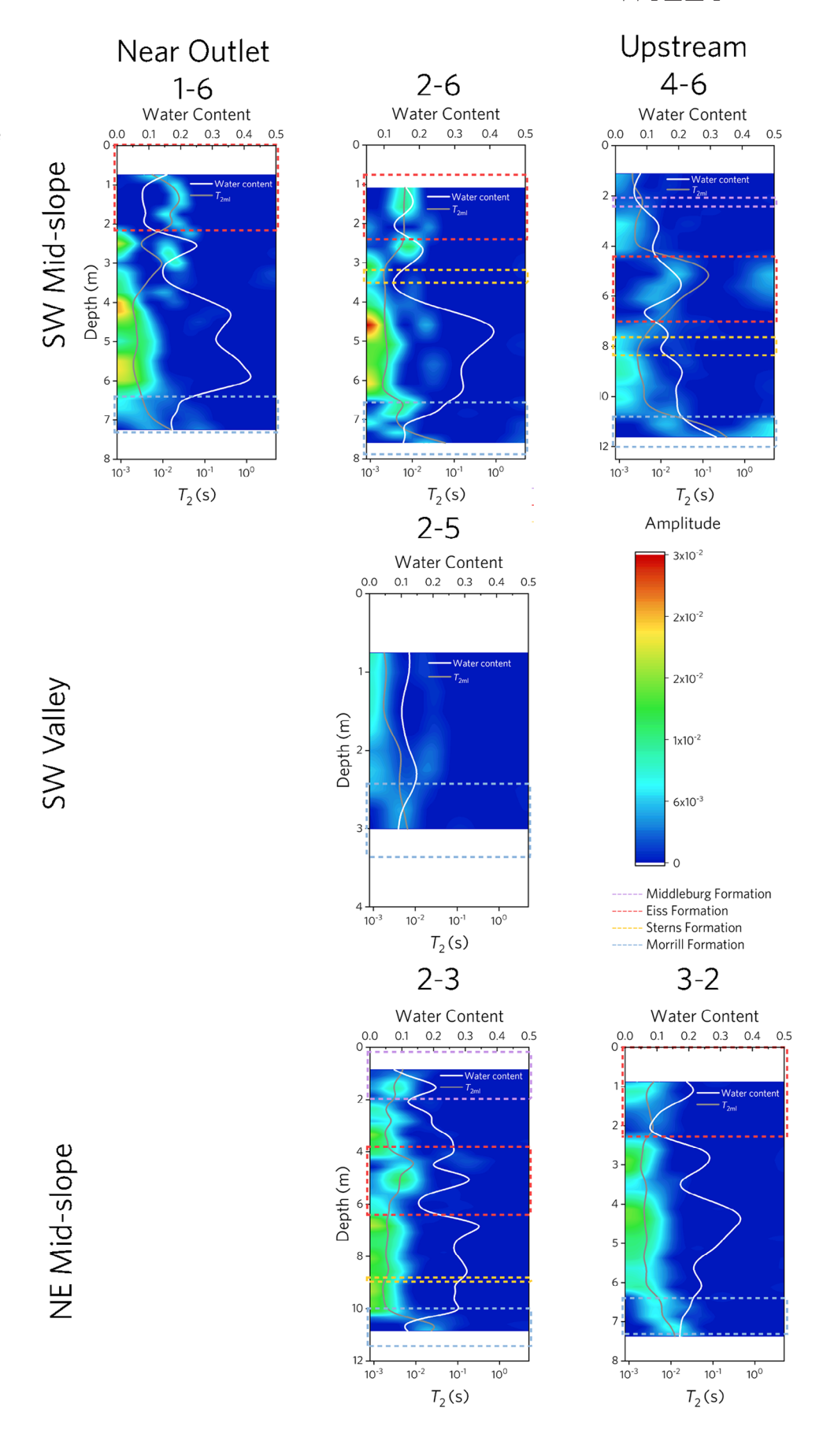
5.2 | Borehole NMR (bNMR)

Results from bNRM are key to validating perceived moisture conditions from spatially extensive 2D ERT profiles, as such we superimposed bNMR results on the ERT profiles (blue lines in Figure 5). Generally we find a correlation of high moisture content as determined by bNMR and low resistivity values observed by ERT. Higher water content in the shale layers (e.g., 20–40%) are associated with resistivities below 25 Ω -m, while low water content (<20%) is present in shales with resistivities between 40 Ω -m and 60 Ω -m. Thus, the pronounced resistivity variation in both shales and limestones indicates that the distribution of water is strongly heterogenous, and localized resistivity minima at shale-limestone contacts suggests zones of increased hydrologic connectivity across lithologic units. We must point out that the collection of ERT and bNMR measurements were separated by months, but drought conditions continued to persist through both survey periods, and thus represent a similar hydrological state.

To better understand the controls on moisture behaviour with depth from the bNMR measurements we focused on the T_2 relaxation time of the differing formations, as longer times indicate larger pores and vice versa (Figure 6; two hillslope positions - mid-slope and valley - on either side of the stream, coloured dashed boxes indicate different formations). The NMR T2 distributions ranged from 0.001 to 5 s (Figure 6) and the inverted volumetric water content (white lines) ranged from 5 to 45% (volume percentage) across the six profiles. The characteristic relaxation time (T_{2ml}), which can be considered representative of characteristic pore size under saturated conditions, is also plotted in the figure (grey lines; Figure 6). For reference, T_2 for bulk water is \sim 2.4 s. In saturated conditions, the T_2 distribution can be used to calculate the pore size distribution. For Eiss limestones in well 4-6, the T₂ distributions are bimodal indicating both micro-secondary pores (tens of milliseconds) and macropores or micro-fracture (few seconds), which can be attributed to processes such as heterogeneous karstification. For many other depth intervals, the T_2 distributions are unimodal, suggesting only one dominant pore type. The shale layers (between the limestone layers) have smaller pores (corresponding to lower T_2) than limestone.

Most of the surveys were taken in the mid-slope position and varied in depth according to each well depth, with well 2-5M being the shallowest at \sim 2.5 m deep and well 4-6M being the deepest at \sim 11 m deep. Based on inverted T_2 distributions the overall water content in the southwest mid-slope profiles first increased at the base of the first limestone, suggesting a perched effect between the limestone and shale. For the 1-6M and the 2-6M wells, water contents were elevated at depth, but these high values coincided with shale layers and relaxation times from the bNMR suggest the majority of the water is clay bound. In the deeper 4-6M, which is known to be in a very hydrologically conductive zone (Figure 3; high saturated hydraulic conductivity and large variance in water table position), mobile water was detected in the upper portion of the Eiss and the Morrill Limestones. In the valley (2-5M), the water content remained fairly homogenous (15%) over the short depth interval, which may be a result of the fact that the well solely represents clay colluvial material (based on core records and surface mapping), and is consistent

FIGURE 6 The T_2 distributions (colour ramp), characteristic relaxation time (T_{2ml} ; grey line), and inverted water content (white line) from six bNMR measurements in the N04d watershed at Konza (location for boreholes are indicated as green circles in Figure 4). The known locations of four limestone units (dashed boxes) are overlain: from youngest (top) to oldest (bottom): Middleburg Limestone (purple), Eiss Limestone (red), Stearns (yellow) discontinuous limestone within the shale, and Morrill Limestone (blue)



with low variability in longer term water table behaviour (Figure 3). While the depth distribution of these wells differs, the general pattern suggests that upstream from the outlet the lithology is holding more mobile water and that this area might have a greater degree of vertical connectivity between units (inferred from the T_2 distribution in 4-6M). Vertical connectivity in the area of 4-6M would also be in accordance with the observation of the local groundwater depression (Figure S1), and higher saturated hydraulic conductivity measurements and greater water table variance (Figure 3).

5.3 | Surface nuclear magnetic resonance (sNMR)

Unlike the bNMR data, which are limited by well depth, sNMR measurements provide vertical profiles averaged over larger areas

(loop size \sim 35 m) to depths up to 30 m below the land surface (Figure 7). The vertical resolution gradually decreased from 0.4 m (the shallowest) to 4 m (at 30 m). However, the top 5–10 m were also subject to high noise (interference from powerlines and thunderstorms). Thus, these data help to validate the deeper ERT measurements (depths >10 m). We only use sNMR results as a relative comparison with bNMR data since the long dead time of our sNMR instrument (10 ms) inhibits capturing water in small pores, resulting in a general underestimation of water content compared to that determined by bNMR (dead time of 0.5 ms).

The inverted water content profiles from the sNMR showed the lowest values for mid-slope profiles (S3 and S4), with a slight increase in water content in upslope locations (S1 and S2), and significantly higher water content in the valley location S7, while other valley locations S5 and S6 have similar water contents as in the upslope

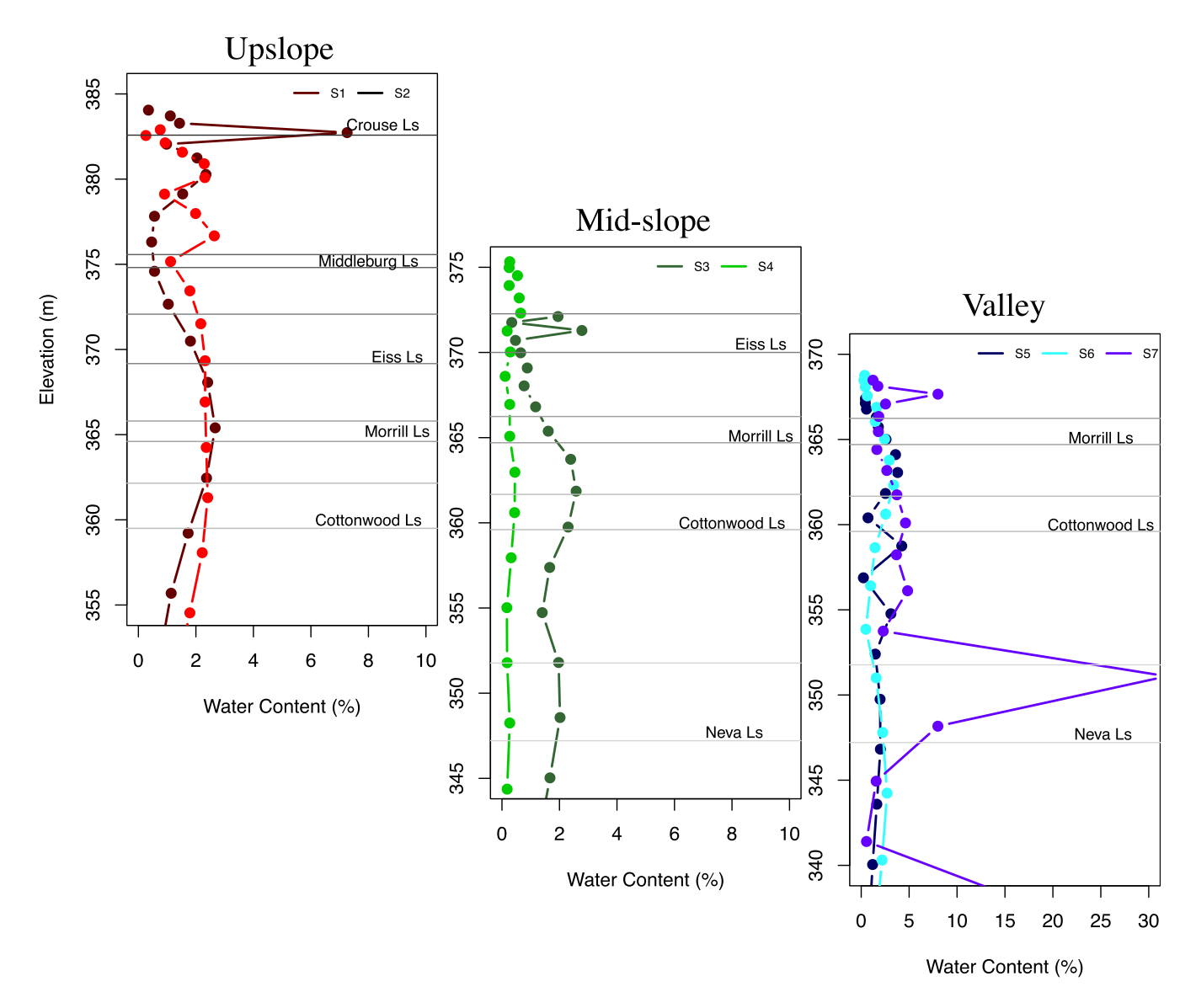


FIGURE 7 The inverted water content from sNMR measurements at seven locations (red diamond; Figure 4) west of the stream at Konza in the NO4d watershed superimposed with the average depths of the known limestones according to their relative hillslope position: upslope (left), mid-slope (centre), and valley (right). Due to difference in landscape position, the elevation can change between sNRM measurements which is why lines may start at different locations (e.g., Mid-slop lines start at two different elevations)

(Figure 7). Generally, the water content was elevated in all surveys near the shallowest shale-limestone boundary (limestone formations indicated in Figure 7), while water content profiles with depth had no uniform pattern. In the valley profile S7 the water content reached a maximum in the Neva Limestone, roughly 20 m below the land surface.

The sNMR measurements S1 and S2 are along the ERT profile P1 at northwest and southeast ends, respectively. The slightly elevated water content between 15 and 20 m depth corresponds to the two zones of decreased resistivity observed in the Eiss formation at both ends. Similarly, where sNMR and ERT measurements were close to each other (S3, S4, and S7), the water content profiling is generally consistent with the resistivity changes (high water content low resistivity). Interestingly areas near the stream had both the highest water contents observed (S7) and the lowest (S4), and the other two valley locations S5 and S6 exhibit low water content especially in the Neva Limestone, attesting to the heterogeneity of this environment. The sNMR measures a relaxation parameter T_2^* , which reflects the mean pore size. The T_2^* is very low at depth (0.0067 s), indicating micropores persist here. Considering both water content and T_2^* data, the drastic difference in the Neva Limestone in the valley suggest strong and localized karstification in this unit at S7 and very well-developed small secondary porosity. It is important to note that the highest moisture content sNMR profile (S7) occurred at a low topographic elevation, where the Eiss Limestone is absent due to erosion, while the lowest moisture content profile (S4) is at a mid-slope position, in an area of known colluvial clay deposits at the surface which may reduce water transmission to depth. Overall these data show that the shallowest limestones at any point contain the most moisture, moisture is probably higher in the intervening shales than in the limestones below the shallowest limestone, and that the Neva Limestone may represent a more regional water table in the valley, but not on the slopes. This latter point highlights the importance of the stream valleys on water movement at this site, in opposition to other studies (e.g., St Clair et al., 2015).

5.4 | Ground penetrating radar (GPR)

Reflectors from GPR captured near-surface changes (<2 m) in lithology between limestone and shale but in most cases were unable to image the variation in the deep structure due to low resistivity (strong EM wave attenuation) within the shale layers. At shallow depths the GPR characterization of different formations was consistent with the ERT results (Figure 8). The reflectors coincide with high resistivities, adding to the interpretation of shallow limestone layers and/or zones of low water saturation as also suggested from ERT. Only in a few locations we found potential hints for laterally consistent reflectors at larger depths (Figure 8). Specifically, diffuse but stronger and laterally coherent reflectivity (e.g., in the centre of the profile P5 below the surface limestone) might be interpreted as increased fracture density and/or karstification, thus also indicating zones of potential crossformation connectivity. However, the ambiguity of the deeper GPR

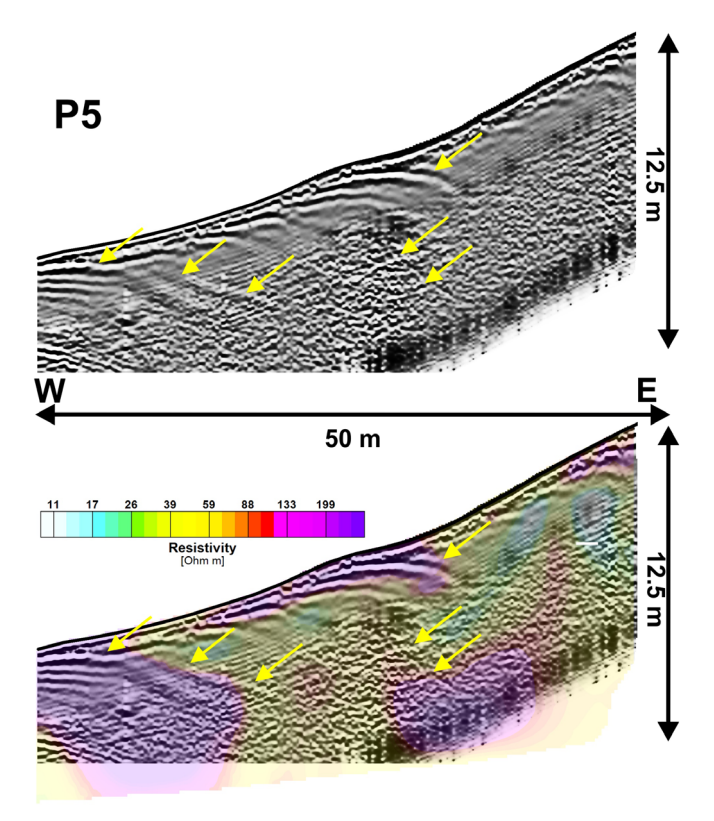


FIGURE 8 Upper panel: GPR image along profile P5 (200 MHz antenna). Fine-scale surface-parallel layers are acquisition and processing artefacts. Yellow arrows show interpreted reflectors, indicating changes in lithology, fracture density/karstification, or water content, Lower panel: Superposition of the GPR image and the electrical resistivity distribution

data due to strong EM wave attenuation does not strictly require such an explanation.

6 | IMPLICATIONS

Multiple geophysical techniques (ERT, sNMR, bNMR, and GPR), constrained with lithologic data from cores, borehole cuttings and groundwater elevations from 25 monitoring wells at the Konza Prairie, were used to evaluate the current conceptual model of hydrologic connectivity in merokarst environments. While "pure" karst systems are known for the generation of deep conduits that can quickly transmit water to great depths and in erratic patterns, merokarst so far were thought to be vertically constrained by alternating shale and more permeable units. These confining layers were hypothesized to create solution-enlarged conduits aligned with the bedding planes, and were thought to be often driven by bi-directional exchange with stream water (White, 1969). Our data suggest that despite limestone units having distinctly different chemistries (Macpherson, 1996; Wood & Macpherson, 2005), downward vertical connectivity between limestone units, first suggested by dye tracer tests (Barry, 2018), likely occur and thus, may control groundwater flow. The vertical connectivity is inferred from the resistivity and NMR water content data, as GPR was not able to unambiguously image the deeper (>2 m) subsurface. From these data we observe that vertical connection is heterogenous in space, occurring upstream, and likely helps to drain water from stratigraphically higher units in the upper portions of the catchment to greater depths, syphoning water that might otherwise flow to the stream (based on dip) to leave the catchment as deep groundwater. Below we discuss: (a) the importance of groundwater export is an unappreciated component of current conceptual models of flow in merokarst, (b) how lateral and vertical variations in the structure of merokarst enhances spatial variability in perched aquifers and thus, controls groundwater flow, and finally, (c) how multiple geophysical measurements offer a toolset that illuminates varying facets of shale-limestone interbeds and their connectivity.

6.1 | Vertical connectivity may play a more important role in groundwater export than is currently appreciated in merokarst

Localized cross-formation low-resistivity zones imaged by ERT (indicated by contrasting colours within the same unit [dotted lines] in P3, P4, P5 in Figure 5) combined with the elevated T_2 distributions and elevated water content detected using bNMR and sNMR support the presence of downward vertical groundwater connectivity, which has the potential to reach much deeper units in this merokarst environment (e.g., Neva limestone >20 m below the surface at Konza; see S7 in Figure 7). It has been long recognized that watersheds, especially those underlain by sedimentary rocks, can support subsurface flow paths where water is exported from one river basin and imported into another (e.g., Frisbee et al., 2016; Hursh, 1946; Schaller & Fan, 2009; Tóth, 1963)-a process often termed interbasin groundwater flow (IGF). Yet, as Frisbee et al. (2016), point out it is challenging to locate and quantify IGF that occurs in any given watershed. Thus, such exports of groundwater are often neglected when understanding the hydrology of watersheds and how they might co-evolve (e.g., Troch et al., 2015) with climate or land-use change. Given this groundwater flux can represent up to 25% of annual precipitation and 10% of mean annual precipitation (Bouaziz et al., 2018), developing more predictive frameworks that account for it is necessary. Here we demonstrated that geophysical tools can help identify locations where IGF may occur. Specifically, ERT and bNMR indicated potential zones of connected moisture with depth (P3, P4, P5 in Figure 5), in what otherwise should be a vertically disconnected system. These verticallyconnected zones occurred along profiles located upstream and coincided with wells that have higher hydraulic conductivity and greater water variance compared to downstream wells (Figure 3). The next step in understanding the position of these vertical connections is to examine how they relate to the local morphology and to determine if there is a consistent geomorphic and geologic interaction occurring that can be quantified and used to predict groundwater-surface water interactions in merokarst.

6.2 | Lateral and vertical structure controls groundwater flow paths: Implications for weathering and evolution of systems

Tóth (1963) patterns of groundwater flow where topography controls local, intermediate, and regional groundwater flow paths may not work at the local scale in merokarst environments where the bedding planes have a very low dip angle. At Konza, the picture that emerges is that upstream vertical subsurface features (indicated by unit resistivity changes in P3, P4, and P5; Figure 5) may support connectivity to deeper units that coincide with the position where potentiometric surfaces indicate the upstream presence of a groundwater depression and a flow of groundwater opposite to the direction of stream flow (see Figure S1). Given this "reversal" of what would intuitively be assumed for groundwater flow in low order headwaters (i.e., groundwater flowing toward the stream) it underscores a need to examine how such flow regimes impact the evolution of porosity and weathering of these subsurface systems over time. Since carbonate systems are highly reactive, infiltrating slightly acidic precipitation or soil-CO2-rich acidic recharge water can enhance dissolution as it enters the subsurface. The degree of weathering and the network of conduits that are derived thus depend on the flow path and depth to which soil CO2 and organic acids are delivered to the subsurface. If the observed trends in NO4d persist in other watersheds in this region, or in other low-order merokarst watersheds with only a slight dip of the bedding plane, then it suggests that porosity may develop to a greater degree near the stream, enhancing rates of channel incision, than compared to environments where groundwater predominately flows toward the stream. Here, observations from several cores at Konza demonstrate that secondary porosity is enhanced near the stream (see Figure S3). If this greater degree of development occurs near branching channels, it may could help to weaken rock, support collapse features, and enhance connectivity between limestone units.

6.3 | Multiple geophysical tools are needed for understanding connectivity in merokarst

Our study demonstrates that a combination of different geophysical tools is necessary to derive robust interpretations of the hydrological patterns in merokarst, in particular when well control or other hard constraints on lithology are lacking. A single-method approach is most likely to fail as the individual techniques are either ambiguous in terms of interpretation (ERT), lack spatial resolution (NMR), or do not deliver results in certain lithologies (shale) and in areas with high water saturation (GPR). Between the two types of NMR measurements, the sNMR allows deeper depth of investigation than bNMR, but the bNMR enhances the detection of water located in small pores in shale units with better vertical resolution. Depending on the noise level, water content values from sNMR might only be used for relative comparison. Here we show the robust total water content information obtained from NMR measurements can be correlated to the in-situ resistivity, and the combination allows at least qualitative insights into

the vertical and lateral distribution of moisture. For example, the superposition of bNMR in well 1-6 on ERT profile P6 (Figure 5) can be used to associate a water content of 40% with a resistivity of about 20 Ohm m in the shale between the limestone units, and consequently the lower resistivities in the same formation toward the southeast indicate an even higher water content. ERT clearly shows pronounced lateral variation of resistivity in both shale and limestone layers, and NMR provides the insight that these shale layers locally host a large amount of water. Both observations support vertical connectivity between different lithologies. Moreover, the NMR T₂ relaxation time distribution indicates the relative pore size changes along the profile, providing evidence of lithology changes at these locations. While at our field site in most instances the strong attenuation of the GPR signal could only highlight lithologic changes within the first 2 m of the subsurface, it might be possible to image larger depths in other lithologies and at different (e.g., drier) conditions. Lower frequency antenna might increase the imaging depth as well, which however comes at the expense of decreased resolution.

To further constrain the structural complexity of karstic limestone we suggest extending our pointwise and 2D acquisitions to three dimensions. This would allow for more accurate processing and interpretation, although the data fit of our 2D resistivity inversions is already remarkably good in light of the heterogeneity of the subsurface. To increase lateral and vertical resolution at known areas of interest, the spacing between electrodes could be decreased helping to constrain spatial extent and degree of vertical connectivity between units. More frequent measurements of both NMR tools would provide better constraints on the moisture content changes observed in ERT and the degree to which this water is more or less mobile, helping to also better constrain vertical connectivity.

Mainly due to logistical constraints, seismic methods have not been applied in this study. However, we suggest incorporating high-resolution reflection seismic and surface wave seismology as they can provide useful constraints on structure and lithology do to their overall lower sensitivity to the presence of subsurface water. The effectiveness of combined geophysical measurements can be maximized by joint inversions of multiple data types based on either structural constraints or explicit petrophysical relationships.

Ultimately, the dynamics of hydrologic patterns over large spatial areas could be directly observed with time-lapse surveys or continuous monitoring, which adds more challenges to the data acquisition and inversion. Focusing on periods where there are typically distinct changes in catchment storage could provide significant insight on subsurface flow patterns. Given the fast recharge dynamics at Konza (Brookfield et al., 2017) such surveys should occur around big recharge events, which tend to occur in the fall when evapotranspiration declines and winter precipitation inputs increase, and during the spring when the system is often moist but before evapotranspiration begins to ramp up. Focusing on areas where vertical connectivity is thought to persist from our initial measurements (e.g., P5) would then allow us to quantify the rate in changes of moisture in the subsurface. Ambiguity arising from lithology in geophysical interpretation could also be eliminated from time-lapse monitoring.

7 | CONCLUSION

Our data show that merokarst exhibits both lateral and vertical heterogeneity and our observations do not support a simplified horizontal flow model. Specifically, the combination of ERT and nuclear magnetic resonance (NMR) at the surface and in boreholes together can be used to identify areas of vertical connectivity across geologic units and where secondary porosity generation (T_2 distributions) may support a greater degree of mobile water connectivity. At Konza, a representative merokarst grassland of the greater Flint Hills, we found that vertical hydrologic connectivity across limestones (~1 m thick) and shales (~2 m thick) is supported by all three types of measurements. Vertical connectivity, possibly driven through karstification and collapse processes lead to groundwater table depressions which in turn support substantial groundwater export, at least during the dry season. These groundwater depressions can re-route groundwater to flow upstream, which co-occurs with enhanced secondary porosity near the stream. Understanding when these connections arise, how long they persist. and their control over the catchment morphological evolution/trajectory and stream discharge remains elusive. What our data reveal is that a systematic approach using multiple geophysical tools and time-laps measurements could unravel these processes over large spatial areas providing data to develop regional morphological rules.

ACKNOWLEDGEMENTS

We thank the Konza Prairie Biological Station, Konza Prairie Long Term Ecological Research (LTER) grant (NSF 1440484) and the University of Kansas (KU) General Research Fund for support. G. L. Macpherson appreciates support from the KU Department of Geology and the Geology Associates Fund. We thank Andrew Parsekian (University of Wyoming) and George Tsoflias (KU) for assisting in NMR and GPR data analysis, respectively. We thank our field geophysical crew for geophysical data collection: Emily Barry, Hussain Bohuliga, James Colgin, Chantelle Davis, Morgan Johannesen, Gang Li, Zalma Tatricia Molina, Alex Nolte, Ling Peng, Joseph Pickert, Yicun Wang, Zhuang Xu, and Bradley James Carr. Chi Zhang and Fan Zhang thank CUAHSI Instrumentation Discovery Travel Grant.

DATA AVAILABILITY STATEMENT

Hydrology and climate data sets were provided by the Climate and Hydrology Database Projects, a partnership between the Long-Term Ecological Research program and the U.S. Forest Service Pacific Northwest Research Station, Corvallis, Oregon. Significant funding for these data was provided by the National Science Foundation Long-Term Ecological Research program and the USDA Forest Service. URL is: https://climhy.lternet.edu/access.html

ORCID

Pamela L. Sullivan https://orcid.org/0000-0001-8780-8501

REFERENCES

Al-fares, W., Bakalowicz, M., Guérin, R., & Dukhan, M. (2002). Analysis of the karst aquifer structure of the Lamalou area (Hérault, France) with

- ground penetrating radar. *Journal of Applied Geophysics*, 51(2-4), 97–106. https://doi.org/10.1016/s0926-9851(02)00215-x
- Ammar, A. I., & Kamal, K. A. (2018). Resistivity method contribution in determining of fault zone and hydro-geophysical characteristics of carbonate aquifer, eastern desert, Egypt. Applied Water Science, 8(1), 1. https://doi.org/10.1007/s13201-017-0639-9
- Barry, E. R. (2018). Characterizing Groundwater Flow Through Merokarst, Northeast Kansas, USA. (M.S.), University of Kansas, Unpublished.
- Bouaziz, L., Weerts, A., Schellekens, J., Sprokkereef, E., Stam, J., Savenije, H., & Hrachowitz, M. (2018). Redressing the balance: Quantifying net intercatchment groundwater flows. *Hydrology and Earth System Sciences*, 22(12), 6415–6434. https://doi.org/10.5194/hess-22-6415-2018
- Brookfield, A. E., Macpherson, G. L., & Covington, M. D. (2017). Effects of changing meteoric precipitation patterns on groundwater temperature in karst environments. *Ground Water*, 55(2), 227–236. https://doi.org/ 10.1111/gwat.12456
- Carrière, S. D., Chalikakis, K., Sénéchal, G., Danquigny, C., & Emblanch, C. (2013). Combining electrical resistivity tomography and ground penetrating radar to study geological structuring of karst unsaturated zone. *Journal of Applied Geophysics*, 94, 31–41. https://doi.org/10.1016/j.jappgeo.2013.03.014
- Coates, G. R., Xiao, L., & Prammer, M. G. (1999). NMR logging: Principles and applications (Vol. 344). Houston, TX: Haliburton Energy Services.
- Costigan, K. H., Daniels, M. D., & Dodds, W. K. (2015). Fundamental spatial and temporal disconnections in the hydrology of an intermittent prairie headwater network. *Journal of Hydrology*, 522, 305–316. https:// doi.org/10.1016/j.jhydrol.2014.12.031
- Dreybrodt, W. (2012). Processes in karst systems: Physics, chemistry, and geology (Vol. 4). Berlin: Springer Science & Business Media.
- Everett, M. E. (2013). Near-surface applied geophysics. Cambridge: Cambridge University Press.
- Fan, Y. (2015). Groundwater in the Earth's critical zone: Relevance to large-scale patterns and processes. *Water Resources Research*, *51*(5), 3052–3069. https://doi.org/10.1002/2015wr017037
- Fan, Y., Clark, M., Lawrence, D. M., Swenson, S., Band, L. E., Brantley, S. L., ... Yamazaki, D. (2019). Hillslope hydrology in global change research and earth system modeling. *Water Resources Research*, 55(2), 1737–1772. https://doi.org/10.1029/2018wr023903
- Ford, D., & Williams, P. D. (2013). *Karst hydrogeology and geomorphology*. West Sussex, England: John Wiley & Sons.
- Frisbee, M. D., Tysor, E. H., Stewart-Maddox, N. S., Tsinnajinnie, L. M., Wilson, J. L., Granger, D. E., & Newman, B. D. (2016). Is there a geomorphic expression of interbasin groundwater flow in watersheds? Interactions between interbasin groundwater flow, springs, streams, and geomorphology. *Geophysical Research Letters*, 43(3), 1158–1165. https://doi.org/10.1002/2015gl067082
- Grant, G. E., & Dietrich, W. E. (2017). The frontier beneath our feet. *Water Resources Research*, 53(4), 2605–2609. https://doi.org/10.1002/2017wr020835
- Grunewald, E., & Knight, R. (2011). A laboratory study of NMR relaxation times in unconsolidated heterogeneous sediments. *Geophysics*, 76(4), G73–G83. https://doi.org/10.1190/1.3581094
- Hartmann, A., Goldscheider, N., Wagener, T., Lange, J., & Weiler, M. (2014). Karst water resources in a changing world: Review of hydrological modeling approaches. *Reviews of Geophysics*, 52(3), 218–242. https://doi.org/10.1002/2013rg000443
- Hartmann, A., Lange, J., Weiler, M., Arbel, Y., & Greenbaum, N. (2012). A new approach to model the spatial and temporal variability of recharge to karst aquifers. *Hydrology and Earth System Sciences*, 16(7), 2219–2231.
- Hayden, B. (1998). Regional climate and the distribution of tallgrass prairie. In A. K. Knapp, J. M. Briggs, D. C. Hartnett, & S. L. Collins (Eds.),

- Grassland dynamics: Long-term ecological research in tallgrass prairie. New York, NY: Oxford University Press.
- Holbrook, W. S., Riebe, C. S., Elwaseif, M., Hayes, J. L., Basler-Reeder, K., Harry, D. L., ... Hopmans, J. W. (2014). Geophysical constraints on deep weathering and water storage potential in the southern sierra critical zone observatory. *Earth Surface Processes and Landforms*, 39(3), 366–380. https://doi.org/10.1002/esp.3502
- Hursh, C. R. (1946). Where little waters write big stories. *American Forests*, 52(12), 574–577.
- Leucci, G., Margiotta, S., & Negri, S. (2004). Geophysical and geological investigations in a karstic environment (Salice Salentino, Lecce, Italy). *Journal of Environmental and Engineering Geophysics*, 9(1), 25–34. https://doi.org/10.4133/jeeg9.1.25
- Lewis, M. A., Cheney, C. S., & O Dochartaigh, B. E. (2006). Guide to Permeability Indices. British Geological Survey, 29 pp. (CR/06/160N) http://nora.nerc.ac.uk/id/eprint/7457/
- Loke, M. H., Chambers, J. E., Rucker, D. F., Kuras, O., & Wilkinson, P. B. (2013). Recent developments in the direct-current geoelectrical imaging method. *Journal of Applied Geophysics*, 95, 135–156. https://doi.org/10.1016/j.jappgeo.2013.02.017
- Macpherson, G. L. (1996). Hydrogeology of thin limestones: The Konza prairie long-term ecological research site, northeastern Kansas. *Journal* of Hydrology, 186(1–4), 191–228.
- Macpherson, G. L., Roberts, J., Blair, J., Townsend, M., Fowle, D., & Beisner, K. (2008). Increasing shallow groundwater CO₂ and limestone weathering, Konza prairie, USA. *Geochimica et Cosmochimica Acta*, 72(23), 5581–5599.
- Macpherson, G. L., & Sullivan, P. L. (2018). Watershed-scale chemical weathering in a merokarst terrain, northeastern Kansas, USA. *Chemical Geology*, 527, 118988. https://doi.org/10.1016/j.chemgeo.2018. 12.001
- Malagò, A., Efstathiou, D., Bouraoui, F., Nikolaidis, N. P., Franchini, M., Bidoglio, G., & Kritsotakis, M. (2016). Regional scale hydrologic modeling of a karst-dominant geomorphology: The case study of the Island of Crete. *Journal of Hydrology*, 540, 64–81. https://doi.org/10.1016/j. jhydrol.2016.05.061
- Martin, J., & White, W. (2008). Frontiers of karst research, special publication 13. Lessburg, VA: Karst Warer Institute.
- Mazzilli, N., Boucher, M., Chalikakis, K., Legchenko, A., Jourde, H., & Champollion, C. (2016). Contribution of magnetic resonance soundings for characterizing water storage in the unsaturated zone of karst aquifers. *Geophysics*, 81(4), WB49–WB61.
- McCormack, T., O'Connell, Y., Daly, E., Gill, L. W., Henry, T., & Perriquet, M. (2017). Characterisation of karst hydrogeology in Western Ireland using geophysical and hydraulic modelling techniques. *Journal of Hydrology: Regional Studies*, 10, 1–17. https://doi.org/10.1016/j.ejrh.2016.12.083
- Müller-Petke, M., Dlugosch, R., Lehmann-Horn, J., & Ronczka, M. (2015). Nuclear magnetic resonance average pore-size estimations outside the fast-diffusion regime. *Geophysics*, 80(3), D195–D206. https://doi.org/ 10.1190/geo2014-0167.1
- Nippert, J. B., & Knapp, A. K. (2007). Linking water uptake with rooting patterns in grassland species. *Oecologia*, 153(2), 261–272. https://doi. org/10.1007/s00442-007-0745-8
- Parsekian, A. D., Singha, K., Minsley, B. J., Holbrook, W. S., & Slater, L. (2015). Multiscale geophysical imaging of the critical zone. *Reviews of Geophysics*, 53(1), 1–26. https://doi.org/10.1002/2014rg000465
- Phillips, J. D. (2018). Self-limited biogeomorphic ecosystem engineering in epikarst soils. *Physical Geography*, 39(4), 304–328. https://doi.org/10.1080/02723646.2018.1456828
- Plan, L., Filipponi, M., Behm, M., Seebacher, R., & Jeutter, P. (2009). Constraints on alpine speleogenesis from cave morphology A case study from the eastern totes Gebirge (northern calcareous Alps, Austria). *Geomorphology*, 106(1-2), 118-129. https://doi.org/10.1016/j.geomorph.2008.09.011

- Ransom, M. D., Rice, C. W., Todd, T. C., & Wehmueller, W. A. (1998). Soils and soil biota. In A. K. Knapp, J. M. Briggs, D. C. Hartnett, & S. L. Collins (Eds.), Grassland dynamics – Long-term ecological research in tallgrass prairie (pp. 48–66). New York, NY: Oxford University Press.
- Redhaounia, B., Ilondo, B. O., Gabtni, H., Sami, K., & Bédir, M. (2016). Electrical resistivity tomography (ERT) applied to karst carbonate aquifers: Case study from Amdoun, northwestern Tunisia. Pure and Applied Geophysics, 173(4), 1289–1303. https://doi.org/10.1007/s00024-015-1173-z
- Robert, T., Dassargues, A., Brouyère, S., Kaufmann, O., Hallet, V., & Nguyen, F. (2011). Assessing the contribution of electrical resistivity tomography (ERT) and self-potential (SP) methods for a water well drilling program in fractured/karstified limestones. *Journal of Applied Geophysics*, 75(1), 42–53. https://doi.org/10.1016/j.jappgeo.2011.06.008
- Robinson, D. A., Binley, A., Crook, N., Day-Lewis, F. D., Ferré, T. P. A., Grauch, V. J. S., ... Slater, L. (2008). Advancing process-based watershed hydrological research using near-surface geophysics: A vision for, and review of, electrical and magnetic geophysical methods. *Hydrologi*cal Processes, 22(18), 3604–3635. https://doi.org/10.1002/hyp.6963
- Schaller, M. F., & Fan, Y. (2009). River basins as groundwater exporters and importers: Implications for water cycle and climate modeling. *Journal of Geophysical Research-Atmospheres*, 114(D4), 1–21. https://doi.org/10.1029/2008jd010636
- Smith, G. N. (1991). Geomorphology and geomorphic history of Konza Prairie Research Natural Area, Riley and Geary counties, Kansas. (M.S. thesis), Kansas State Univ., 122 pp.
- Srinivasa Gowd, S. (2003). Electrical resistivity surveys to delineate groundwater potential aquifers in Peddavanka watershed, Anantapur District, Andhra Pradesh, India. Environmental Geology, 1(1), 1–1. https://doi.org/10.1007/s00254-004-1023-2
- St Clair, J., Moon, S., Holbrook, W. S., Perron, J. T., Riebe, C. S., Martel, S. J., ... Richter, D. (2015). Geophysical imaging reveals topographic stress control of bedrock weathering. *Science*, 350(6260), 534–538. https://doi.org/10.1126/science.aab2210
- Sullivan, P. L., Macpherson, G. L., Martin, J. B., & Price, R. M. (2019). Evolution of carbonate and karst critical zones. *Chemical Geology*, 527, 119223. https://doi.org/10.1016/j.chemgeo.2019.06.023
- Tóth, J. (1963). A theoretical analysis of groundwater flow in small drainage basins. *Journal of Geophysical Research*, 68(16), 4795–4812. https://doi.org/10.1029/JZ068i016p04795

- Troch, P. A., Lahmers, T., Meira, A., Mukherjee, R., Pedersen, J. W., Roy, T., & Valdés-Pineda, R. (2015). Catchment coevolution: A useful framework for improving predictions of hydrological change? Water Resources Research, 51(7), 4903–4922. https://doi.org/10.1002/2015wr017032
- Walsh, D. O. (2008). Multi-channel surface NMR instrumentation and software for 1D/2D groundwater investigations. *Journal of Applied Geophysics*, 66(3–4), 140–150. https://doi.org/10.1016/j.jappgeo.2008. 03 006
- Weary, D. J., & Doctor, D. H. (2014). Karst in the United States: A digital map compilation and database: US Department of the Interior, US Geological Survey.
- White, W. B. (1969). Conceptual models for carbonate aquifers. *Groundwater*, 7(3), 15–21. https://doi.org/10.1111/j.1745-6584.1969.
- Wood, H. K., & Macpherson, G. L. (2005). Sources of Sr and implications for weathering of limestone under tallgrass prairie, northeastern Kansas. Applied Geochemistry, 20(12), 2325–2342. https://doi.org/10. 1016/j.apgeochem.2005.08.002
- Zhu, J., Currens, J. C., & Dinger, J. S. (2011). Challenges of using electrical resistivity method to locate karst conduits—A field case in the inner bluegrass region, Kentucky. *Journal of Applied Geophysics*, 75(3), 523–530. https://doi.org/10.1016/j.jappgeo.2011.08.009

SUPPORTING INFORMATION

Additional supporting information may be found online in the Supporting Information section at the end of this article.

How to cite this article: Sullivan PL, Zhang C, Behm M, Zhang F, Macpherson GL. Toward a new conceptual model for groundwater flow in merokarst systems: Insights from multiple geophysical approaches. *Hydrological Processes*. 2020;34: 4697–4711. https://doi.org/10.1002/hyp.13898